THE TUNABLE XUV IMAGER (TXI) SOUNDING ROCKET PAYLOAD

NASA Grant NAG5-5075

Final Report

For Period 6 May 1996 through 31 July 2004

Principal Investigator
Dr. Leon Golub

July 2004

Prepared for:

National Aeronautics and Space Administration
Washington, DC 20546

Smithsonian Institution
Astrophysical Observatory
Cambridge, Massachusetts 02138

NAG5-5075

The Tunable XUV Imager (TXI) Sounding Rocket Payload

FINAL REPORT

PROGRAM ELEMENT: Solar Physics

TECHNIQUE/RESEARCH AREA: Suborbital/Corona

PRINCIPAL INVESTIGATOR:
Dr. Leon Golub, Astrophysicist
Smithsonian Astrophysical Observatory
60 Garden Street, MS 58
Cambridge, MA 02138
(617) 495-7177

INSTITUTIONAL AUTHORIZATION:

SUMMARY

TITLE: The Tunable XUV Imager (TXI) Sounding Rocket Payload

P.I.: Dr. Leon Golub, Smithsonian Astrophysical Observatory

The TXI was flown successfully on 21 June 2001 (36.199 US). All systems functioned as planned and image data were acquired and sent to the ground. Unfortunately, due to a parachute failure the payload was destroyed. In this report we summarize results from the flight and provide detailed information on the high resolution X-ray imaging detector which was developed as part of the program.

The following are selected refereed publications from our rocket program, including the TXI, to date:

Golub, L., E.E. DeLuca, M.A. Weber and A. Sette 2004, *Proc. IAU Symposium 223*, eds. Stepanov *etal.*

"High Resolution Coronal Imaging With Multilayers," *Adv. Space Res.*, 29, 12 (2002).

"Analysis and Comparison of Loop Structures Imaged With NIXT and Yohkoh/SXT," *A. & A.*, 342, 563 (1999).

Golub, L. 1997, "Difficulties in Observing Coronal Structure," *Sol. Phys.*, **174**, 99.

Golub, L. 1996, "The Solar X-ray Corona," *Astrophys. & Space Sci.* **237**, 33.

Yoshida, T., Tsuneta, S., Golub, L., Strong, K. and Ogawara, Y. 1995, "Temperature Structure of the Solar Corona: Comparison of the NIXT and *Yohkoh* X-ray Images," *PASJ* **47**, L15.

Schmieder, B., L. Golub & S.K. Antiochos 1994, "Comparison Between Cool and Hot Plasma Behavior of Surges," *Ap. J.*, **425**, 326.

Peres, G., F. Reale and L. Golub 1994, "Loop Models of Low Coronal Structures Observed by NIXT," *Ap. J.* **422**, 412.

Gary, D.E., Leblanc, Y., Dulk, G.A. and Golub, L. 1994, "The Magnetic Field Above Sunspots," *Ap. J.* **412**, 421.

Sams, B.J., III, L. Golub & N.O. Weiss 1992, "NIXT X-ray Observations of Sunspot Penumbral Structure," *Ap. J.* **399**, 313.

Beaufume, P., B. Coppi & L. Golub 1992, "Coronal Loops & Current-Based Heating," *Ap. J.* **393**, 396.

Spiller, E., *et al.* 1991, "Normal Incidence Soft X-ray Telescopes," *Opt. Eng.* **30**, No. 8, 1109.

Golub, L., *et al.* 1990, "Subarcsecond Observations of the Solar Corona," *Nature* **344**, 842.

Table of Contents

1 Scientific,Technical & Management

1.1 Scientific Objectives

In this section we describe the program of scientific studies to be carried out with the Tunable XUV Imager (TXI) payload. The instrumentation is described in the Sec. 1.2.

NASA's Living With A Star (LWS) and Sun-Earth Connections programs are implementing a core program of solar studies relevant to the interests of the U.S. in general and of NASA in particular. Some of the goals of these programs will be addressed by a U.S.-Japan collaboration on the Solar-B mission and the partially contemporaneous Solar Dynamics Observatory and the STEREO Mission. However, recent studies (discussed below) indicate that observations which are not part of the current plan are need. High spatial resolution observations in multiple wavelengths covering a broad temperature range with good temperature discrimination are crucial to further progress in understanding coronal heating and dynamics. We therefore feel that it is worthwhile to pursue rapid, low-cost missions which can be done within the scope of the NASA Suborbital Program, and which take advantage of recent technological progress in order to construct a new generation of instruments which offer the possibility of advancing LWS/SEC goals in a timely manner, especially in areas not included in the present mission complement.

This proposal describes instrumentation which has been built and flown in an initial low-resolution test flight and which fits these criteria in a high-quality, low-cost package. By rebuilding the already-tested and qualified payload and bringing the full-resolution version to completion we will make available within a short time-frame a new type of instrument whose design takes into account the most recent findings in coronal physics, with the aim of advancing not only LWS and SEC science objectives, but also coronal physics in general.

Our group has, for the past two decades, been engaged in a comprehensive program of solar studies encompassing observations, modelling and theory. We rely on a small core group of in-house staff, while taking full advantage of collaborative arrangements with outside experts as needed for succesful completion of the scientific studies. A crucial part of our program is the availibility to the theoretical and modelling efforts of basic new observational data. This has in large part been accomplished by construction and flight of new instrumentation – such as the NIXT rocket and the *TRACE* and Solar-B XRT telescopes – which can provide the necessary input to the modelling and the necessary constraints on theory.

Below we provide a brief overview of problem areas in coronal physics which we feel to be most pressing, which most need to be addressed in order to advance our understanding of coronal strucutre, stability and dynamics, and for which new types of observational capabilities are needed. We also discuss how the new data which we will obtain from flight of the TXI rocket payload will help to solve the problems which are now facing us.

1

1.1.1 Coronal Heating, Loop Fine Structure and the Multithermal Corona

The region in the Sun's atmosphere between the photosphere and lower corona is one of a very rapid transition in physical parameters: the plasma β (the ratio of gas pressure to magnetic pressure) falls off from roughly unity in the photosphere to about 0.01 in the corona, while the magnetic filling factor increases by the same ratio. The temperature increases by more than two orders of magnitude, and the density decreases by the same amount. This all happens in a layer from 2000 to 5000 km (Aschwanden et al. 2002) across. Observations indicate that this boundary layer is very dynamic and variable, the most dynamic region of the Sun. Its morphology is unknown: it is probably not a true layer, but a zone of separate magnetic structures with different plasma temperatures. Below this region, in the interior of the Sun, the generation of the magnetic field takes place, and above it, in the solar corona, rapid and intense release of magnetic field energy leads to the emission of gamma rays, hard X-rays, and energetic particles up to the energy of cosmic ray particles. All the energy that heats the overlying corona and fuels the massive eruptions and flares must be transported through this region of the solar atmosphere.

Theoretical models have focussed in recent years on the various ways in which energy may be transported to the corona, and there dissipated, through the mediation of magnetic fields. Virtually without exception, these models have in common the feature that the actual dissipation of energy transported to the corona occurs in spatially highly localized regions, which may however either be truly localized or distributed throughout a larger volume. There is also observational support for the presence of unresolved fine structure in the corona, based on studies using density-sensitive line ratios (e.g., Dere et al. 1987; Linford & Wolfson 1988; R. Thomas 1995, personal communication), which typically yield filling factors of 0.01-0.001 for the transition region and corona.

Figure 1: Coronal fine structure at 1 arcsec resolution. Active region seen in Fe IX/X with the TRACE imager, 19 May 1998.

The new data from the TRACE satellite, as shown in Fig. 1, are beginning to resolve this substructure. The localized heating regions implied by these observations are far smaller than the coronal structures which have until now been observed, leading to the ancillary problem of having to explain how the energy which is released can be transported throughout the volumes which need to be heated.

2

A clue to the process by which coronal loops are heated may be provided by the new TRACE high resolution XUV data. Fig. 2 shows the brightening of a structure which, in lower resolution images, would have been called a "loop." The right-hand frame shows that the loop is actually composed of numerous fine threads of bright material, and the two frames at left show the way in which this "loop" brightened: a central bright filament forms, which is then accompanied by other bright parallel filaments; these brighten all along their lengths at once, rather than as a wave of brightness down from the top or up from the bottom. The broadening of the structure as it brightens is actually due to the successive formation of numerous bright filaments parallel to the original one, so that problem of cross-field transport may be avoided.

We believe that these data indicate coronal heating via currents, which would explain the brightening all along the length of the bundle of "threads" (it can no longer be called a "loop"). The formation of additional bright threads parallel to the first one may indicate heating by return currents, which are thought to be necessary in current heating models or in models that invoke a quasi-separatrix layer. The problem now becomes one of explaining why certain bundles of field lines become activated and how the energy deposition within a restricted class of field lines takes place. It appears to be TRACE's high spatial resolution combined with its ability to isolate a narrow temperature range that makes these new observations possible. This capability is shared by the TXI, but will now be extended to ionization states not reached by the SOHO EIT instrument or by TRACE.

A number of recent studies (Yoshida et al. 1995; Takeda et al. 1995; Walker et al. 1993) have emphasized the importance of thermally differentiated imaging of the coronal plasma as part of the program to understand the heating and structuring of the solar corona. It has long been known that very different structures are seen in ground-based eclipse data in, e.g., the 'red line' (Fe X) compared with the 'green line' (Fe XIV) (see e.g., Takeda et al. 1994). In soft x-ray observations, this point has been summarized by noting that the observed coronal loop structures may be viewed as relatively isolated mini-atmospheres (Rosner et al 1978), each with its own temperature and density structure. Because of the marked difference in observed coronal parameters within small spatial distances, it appears that the coronal heating mechanism can have markedly different effectiveness in portions of the atmosphere which are otherwise indistinguishable. The result is that data taken in emission lines of the same element at only slightly different formation temperatures can show very different structures. The point is explicitly demonstrated by the TRACE observations, such as the comparison below of an Fe IX/X view of the corona (left-hand panel), with Fe XII (right-hand panel); the difference in temperature is only $\log T \sim 0.2$.

It is effectively impossible to determine temperatures by passband ratios if the same structures are not seen in the two passbands, and if we do not observe enough temperature intervals to see all of the structures. This problem is solved by the TXI in the temperature range

3
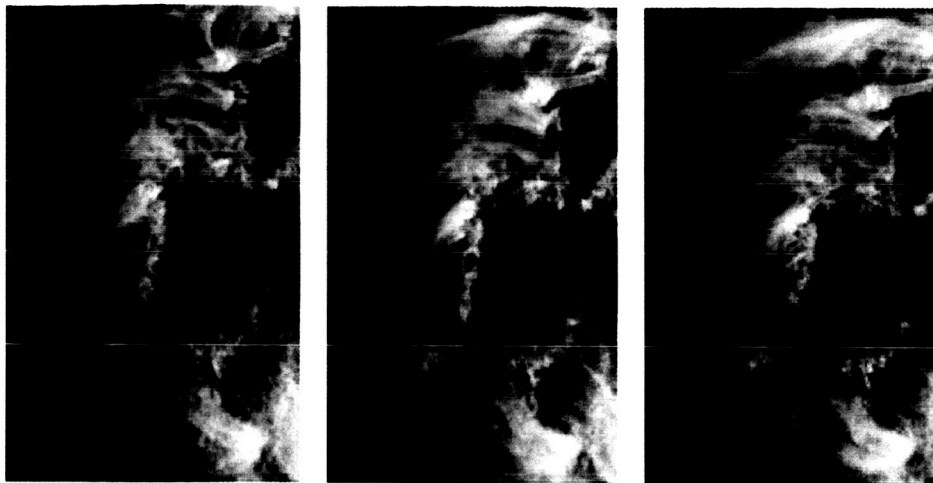
Figure 2: A sequence of images taken in the TRACE 173Å passband, showing a loop brightening event with multiple fine threads of emission. Time between frames is ≈10 min., FOV ~1X2 arcmin. This passband includes both Fe IX and Fe X, which may cause some blurring. The new TXI instrument images each line separately.

$\log T \sim 5.8-6.4$ by our ability to image *all* of the ionization stages from Fe IX through Fe XIV. The plasma has, in effect, nowhere to hide.
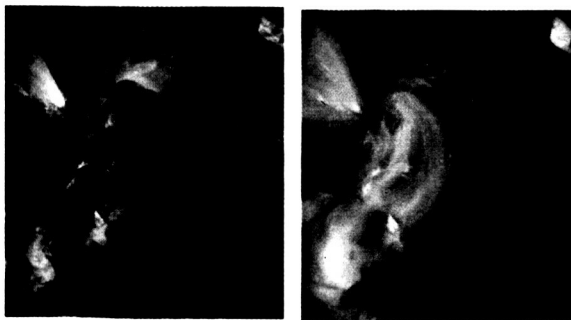
Figure 3: Detail of TRACE Fe IX/X (left) and Fe XII (right) views of an active region, showing strong differences in coronal structure with only a small difference in temperature.

1.1.2 Plasma Flows in the Corona

The question of steady flows in coronal loops has been widely studied starting with Meyer and Schmidt (1968) (see also Glencross (1980), Cargill & Priest (1980), Noci (1981) and Landini & Monsignori Fossi (1981)). Considering mass-conserving flows from one side of a loop to the other, the fundamental conclusion is that flows will arise whenever the loop is subjected to asymmetric heating or a pressure gradient from one footpoint to the other. For small pressure differences the flows remain subsonic, and the structure of the loops is not substantially changed by the presence of a flow. As the forcing is increased, the flow speed increases until the velocity reaches the sound speed at a point (the critical point) in the tube. The downstream velocity is then supersonic.

The observations of flows in coronal loops

have been restricted to lines in the chromosphere, where the flows are necessarily small (Craig and McClymont, 1986). At coronal heights and coronal temperatures flows of several hundred km/s are expected. High-cadence timelapse movies from the TRACE satellite show persistent outflows at the sound speed in long coronal loops emanating from the vicinity of sunspots, while comparison with the SOHO/CDS provides spectroscopic evidence of flows (Winebarger etal. 2001).

With the TXI we will be able to form spatially resolved velocity maps of the entire corona at wavelengths such as 180Å (Fe XI) and 211 Å (Fe XIV), which are particularly well-separated from other strong lines. This is accomplished by positioning the variable narrow passband so that it is alternately leading and trailing the position of the emission line. A line shift due to line-of-sight velocity then causes a change in strength in the two images whose sign depends on the direction of the velocity and whose magnitude depends on the magnitude of the velocity; the difference between the two images then provides a measurement of the velocities. In this manner the amplitude, spatial distribution and temporal evolution of flows in the corona will be directly mapped for the first time. For the bright regions, where we expect 1% relative photometric accuracy between frames, we resolve flows as small as 50 km/sec, comparable to the velocities seen in the TRACE movies.

As an added bonus, we note that the monochromator mirrors operate near the Brewster angle, so that only the σ-polarized component is reflected. The polarization of the XUV emission can therefore be measured simply by rotating the payload 90° around the line-of-sight. This is easily done with the pointing system available at White Sands. The difference image in this instance directly measures the polarization, if any is present.

Summary

We have built and flight-tested a new sounding rocket payload which can provide the next step in observational capability needed to carry out a timely and innovative series of coronal studies, as we have described above. Because the payload was destroyed by a parachute failure before our scientific objectives could fully be met, we are proposing to rebuild and continue flying the payload. The Tunable XUV Imager (TXI) will obtain non-overlapping, spectrally resolved images of the corona in *all* of the emission lines formed at temperatures from <1 MK to >3 MK, including – for the first time – velocity and polarization images of the EUV corona.

As has traditionally been the case with sounding rocket payloads, we view this instrumentation as having both intrinsic scientific merit and as a test bed for future satellite instruments. The proposed investigation is a valuable complement to the SOHO and TRACE science, and it will provide a major addition to the LWS and SEC programs. The flight of the high-resolution TXI will take place near Solar minimum, with a scientific program emphasizing quiet coronal studies and bright points.

5

Figure 4: Image of the EUV corona in the Ni XVII line formed at 3 MK, obtained in the 21 June 2001 flight.

1.2 Technical Approach

The Tunable XUV Imager (TXI) will provide high resolution spectrographic observations of the solar atmosphere from the transition region to active region temperatures. The scientific merits of these observations have been discussed above; here we provide a description of the instrumentation which is being built to carry out this scientific program.

The problems associated with observing the multi-temperature corona imply that the instrumentation which is used must be able to: a) cover a wide range of temperatures, and b) isolate a narrow temperature interval within the broad range. Both of these requirements are met by the Tunable XUV Imager, which provides non-overlapping high resolution spectroheliogram images in individual coronal emission

lines. This is accomplished by using soft x-ray multilayer coatings, which provide high reflectivity at large reflectance angles which until recently were not accessible in the spectral region shortward of ~ 300Å.

The TXI consists of a broadband multilayer coated imaging optic, which is an f/20 on-axis sphere specially coated for a broad wavelength response by Dr. David Windt of Columbia University. Within the broad passband, a narrow wavelength slice is selected by a pair of narrow band analyzer elements; these are identically coated flat mirrors arranged as a Cowan-Golovchenko (Cowan 1983) double crystal monochromator (Figs. 5,7).

The broadband response of the imaging element, and the tunable analyzer bandwidth within that passband, are shown in Fig. 6; note that the mirror pair gives ≈ 1.6 times narrower bandwidth than either element alone, thereby providing spectral resolution adequate to separate the strong Fe lines in the TXI passband. The geometry of the Cowan-type monochromator has the highly desirable property that, with a single drive element the mirrors move automatically in such a way that the entrance and exit beams remain fixed, so that there is no image motion in the focal plane during wavelength selection. The physical and optical parameters of the TXI are listed in Table 1.

In order to meet the scientific goals of the investigation, we have selected the wavelength range $\lambda 171 - 211$Å, which includes strong spectral lines ranging from O V (log T = 5.4) through Fe XXIV (log T = 7.3). A listing of the strongest lines in the TXI range is provided

6
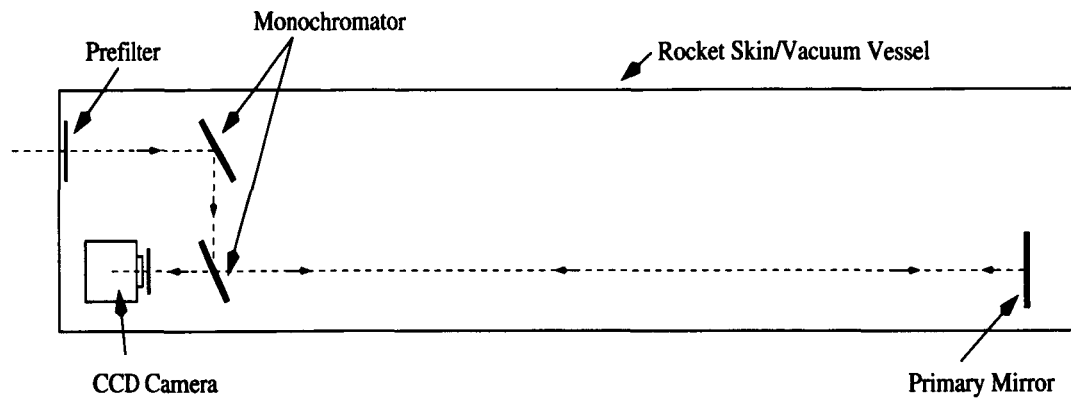
Figure 5: TXI instrument layout, showing entrance filter, double-crystal monochromator, broad-band focussing optic and CCD camera.
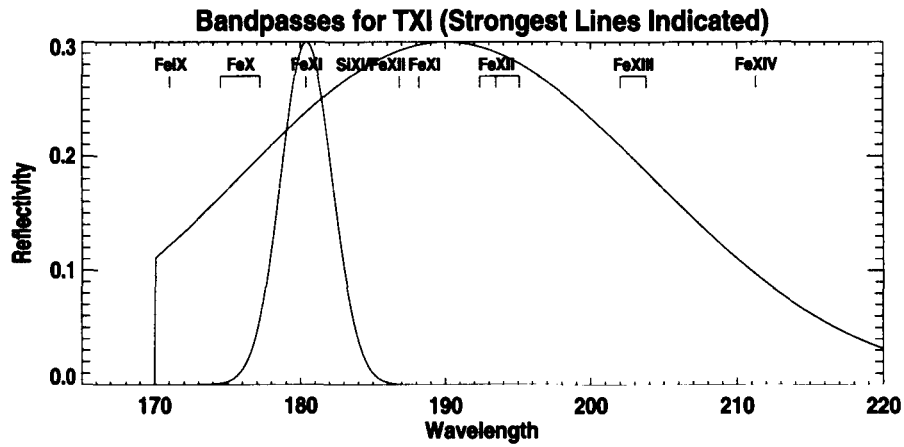
Figure 6: TXI broad and narrow passbands, with the most prominent XUV emission lines indicated.

in Table 2.2. The count rates listed are for active regions and include all mirror reflectivities, polarization effects and filter transmissions, thus representing true focal plane intensities. The backside thinned CCD sensor used in our HRX camera has a DQE of $\approx 80\%$ in the 40–70 eV energy range.

The most prominent lines in the TXI spectral range are those of Fe IX through Fe XIV. They are well-separated in wavelength, so that 'clean' imaging will be achievable. In addition, spectral separation substantially higher than the FWHM of the analyzer elements will be achieved by differential measurements taken with a $\Delta\lambda \sim 1$Å. Given the strengths of the lines involved, the available exposure times and the analyzer element bandwidth of $\Delta\lambda \sim 4$Å, we estimate that all of the lines listed in Table 2.1 can be isolated at the 1% separation level. The He II line at $\lambda 304$Å will be strongly reduced by the three-

7

Physical & Optical Parameters of the TXI	
λ Range:	171-210Å @ 10% of peak
	171-230 @ 1% of peak
Analyzer $\Delta\lambda$:	4 Å
Collecting Area:	75 cm^2 geometric
	2.5 cm^2 eff. area @ peak
Focal Length:	2.2 meters
Detector Resolution:	2K x 2K
Pixel Size:	0.8 arcsec
Exposure Times:	1-3 secs./wavelength
	10 sec @ selected λs

Figure 7: Optical bench portion of the TXI instrument, including entrance aperture, cooling block, CCD camera and XUV monochromator.

reflection system; however, any residual intensity can be calibrated by moving the analyzer mirrors to the second order position at $\sim$152Å. We note also that the presence of multiplets, such as the three closely-spaced lines of Fe XI near 193Å, will not cause image smearing since there is no spatial dispersion in this instrument.

A schematic diagram of the TXI is shown in Fig. 5. The monochromator portion contains a pair of mirrors which will operate in parallel at angles near 45°. At smaller near-grazing angles, the angular size of the sun would cause wavelength mixing which dilutes the monochromator resolution. At near-normal incidence settings, large mirror motions are needed to accomplish wavelength changes and, more subtlely, the rapidly varying π-polarization reflectivity creates a difficult calibration problem. Mirror settings near the Brewster angle sacrifice half of the reflectivity on the first reflection (and none thereafter) but provide stable polarization, clean spectral selection and mirror motion of only ±12°. The as-built monochromator is shown in Fig. 7.

In addition to the pure spectral imaging, the TXI can also provide line-of-sight velocity measurements by alternately positioning the steep positive and negative gradients of the multilayer response function at the wavelength of a given spectral line. The Doppler shift then causes the line to move up or down the reflectivity curve and the difference between the two images is a Doppler image; the sum is equivalent to the on-band image. For a relative photometric accuracy of 1% in the difference images, we will be able to measure line-of-sight velocities of 50 km/sec, which compares favorably with the $\sim$100 km/sec motions we are seeing in the *TRACE* data.

We note also that the operational wavelength range of the TXI can easily be changed by switching out the mirror elements. Thus, on subsequent flights we have the option of moving to other spectral regions (e.g. λ250-400Å) in order to satisfy an extended set of scientific objec-

Strongest Emission Lines Within the TXI Passband

Ion	λ (Å)	$\log T$	Countrate (cts/pix/s)	e^-/pix/s
Fe IX	171.08	5.9	360	8700
O V	172.17	5.4	44	–
O VI	172.94, 173.08	5.5	30	–
Fe X	174.53, 177.24	6.0	390, 240	9200
Fe XI	180.42	6.1	950	2.2×10^4
Si XI/Fe XII	186.88	6.2	770	1.7×10^4
Fe XI	188.22	6.1	670	1.5×10^4
Fe XXIV	192.03	7.3	variable	variable
Fe XII	192.40, 193.52, 195.13	6.2	1300, 680, 630	3×10^4
Fe XIII	202.04, 203.82	6.2	310, 290	1×10^4
Fe XIV	211.32	6.3	180	3500

tives. For mechanical reasons the tuning range of the TXI monochromator section is limited to a factor of two between lowest and highest wavelengths in the flight version; other factors, such as locations of desirable spectral lines, availability of light-blocking filter materials, and multilayer coating performance, also must be taken into account.

1.3 Observing Program.

The scientific program for the TXI has three main observational objectives:

- Obtain high spatial resolution spectroheliogram images with good signal-to-noise in the series of iron lines from Fe IX at λ171 through Fe XIV at λ211Å. Eight wavelength settings are needed and exposure times of 0.1, 1 and 3 seconds are taken at each.

- Obtain deep exposures for some weaker lines in order to extend the temperature range covered; exposures of 10 second duration will be taken at O V and O VI.

- Obtain exposures at intermediate wavelengths for spectral separation and Doppler shift measurements; eight 3-second exposures for this objective.

The total available observing time for our previous rocket flights has averaged 320 seconds, with a minimum of $\approx$300 and a maximum of $\approx$350. The CCD camera can be read out while the monochromator is moving to the next position, since both activities require about the same amount of time (4 secs). The total observing program outlined above will require 240 secs. to complete, which is consistent with the typical minimum time above altitude for White Sands launches, and falls well within the expected duration of solar fine pointing. If estimated sun-acquired times are longer, we will obtain deep exposures at selected wavelengths, in order to image the corona beyond 1.5$R_\odot$.

9

2 Differential Emission Measure (DEM) Determination

Extensive effort has been put into developing methods for reconstruction of the amount of emitting material in the corona as a function of temperature (the DEM) from observations such as those provided by the TXI instrument. These results have been presented at several conferences and a paper has been submitted for publication (Golub etal. 2004).

2.1 Two methods for DEM reconstruction

The differential emission measure (DEM) is a basic observable of the coronal plasma in a region of interest dV. The DEM is a measure of the amount of emitting plasma:

$$\int n_e^2 \, dV = \int \mathrm{DEM}(T) \, dT \, , \qquad (1)$$

where n_e is the electron number density. The intensity d_i observed in channel i is

$$d_i = \int \mathrm{DEM}(T) \, r_i(T) \, dT \, , \qquad (2)$$

where $r_i(T)$ combines the known information, i.e., the temperature response function for channel i with the plasma emissivity function. The DEM may be found, in principle, by inverting Eq. 2, but that is an ill-conditioned problem if the $r_i(T)$ overlap in temperature coverage (as they do for the XRT and AIA). We discuss two approaches to solving this inversion problem: an iterative search method, and inversion methods.

2.2 Iterative methods

We wish to find the "best" fitting DEM for a given set of observations in several spectral channels. Here we consider a set of images taken of an active region (AR). We assume that the structure of the AR loops is unchanged during the time it takes for the instrument to accumulate all of the images. Before processing, the set of images is co-aligned and reduced to physical units (e.g., DN/s). In this section, we discuss how we estimate the DEM in a given pixel. Our procedure produces an iterative least-squares fit to the observations using a DEM represented by a spline with evenly spaced knots in $\log T_e$ space. For the set of observations (all i) in pixel p, we wish to solve the simultaneous equations of Eq. 2. With the forward modeling approach, we assume a starting DEM, apply Eq. 2, and compare the predicted observations for each filter with the real observations. The optimal DEM spline is found using IDL mpfit routines from Craig B. Markwardt which search towards a minimum χ^2 statistic by varying the spline knots. These routines use the non-linear least-squares method based on the MINPACK-1 routines (http://www.netlib.org/minpack/). This method, including uncertainty analysis, is described in more detail in Golub etal 2004.

2.3 Direct inversion methods

Another class of solution methods is comprised of inversion algorithms. Eq. 2 can be written in matrix form as

$$R_{iT} \, \mathrm{DEM}_T = d_i \, , \qquad (3)$$

representing a simultaneous set of linear equations, where DEM_T is a vector of length N_T, and d_i is a vector of length N_i. For $N_T = N_i$, the system is determined and there is a unique solution (assuming no degeneracies in the response

functions). The inversion is easily solvable with standard linear algebra techniques (*e.g.*, lower-upper decomposition). However, unless the selection of temperature bins (implicit in the response functions) happens to be closely consistent with the characteristics of the "true" DEM function, the solution DEM is often unphysical. For example, solution functions often show significant negative DEM values. Furthermore, the constraint $N_T = N_i$ may imply poor resolution in temperature.

For $N_T > N_i$, the system in Eq. 3 is underdetermined, and there is an infinite family of solutions. In other words, the *a posteriori* information (*i.e.*, the data) is insufficient to constrain the model to a unique solution. In this case, there is freedom to constrain the solution with *a priori* information (*i.e.*, physical constraints, such as assumptions about positivity or smoothness). Regularization methods turn Eq. 3 into a well-posed minimization problem with the addition of such a constraint, by trading the quality of fit to the data against the quality of fit to the assumed constraint. (The amount of trade-off is typically adjusted such that the χ^2 fit to the data is $\sim N_i$.) Note that this approach requires an explicit choice of *a priori* assumptions.

Without making any *a priori* assumptions, the method of singular value decomposition (SVD) can be used to describe the family of solutions to Eq. 3. If R_{iT} is considered as a linear map from the DEM space of N_T dimensions to the data space of N_i dimensions, then the SVD algorithm provides the N_i DEM orthonormal basis functions which solve Eq. 3. This reduces the inverse problem to a square

system of equations with a determinable principal solution. SVD also provides $(N_T - N_i)$ DEM orthonormal null-space functions, which add to the principal solution to generate the infinite family of solutions to Eq. 3. (Note that there is no *physical* significance inherent to the principal SVD solution, although it happens to be the solution vector of shortest norm.)

2.4 Comparing DEM reconstruction methods

We compared the iterative and SVD (inversion) methods to evaluate their pros and cons for implementation of an automated algorithm. A variety of nine input DEMs were designed and folded through the AIA response functions to produce simulated observations. Then each set of observations was solved for a reconstructed DEM using three methods: (a) "Simple" inversion (where $N_T = N_i$); (b) SVD principal inversion; and (c) the iterative approach. The "Simple" inversion method was included as a baseline for comparisons, even though it was expected to produce relatively poor reconstructions. We used six of the AIA's EUV channels ($N_i = 6$), and solved for DEMs with $N_T = 19$ temperature bins spanning the range $\log T = 5.6\text{--}7.4$. We have quantified three measures on the relative value of the three solution methods considered. These are recorded in Table 1. The first quantity is runtime. For each set of observations, we calculated the average runtime of the method for 100 runs on a Sun Ultra 10 workstation, with a 440 MHz processor and 1.0 GB of RAM. As expected, the inversion methods are substantially faster than the iterative approach: τ(iterative)

11

DEM model ⇒	a	b	c	d	e	f	g	h	i	Median
Table 1.1: Runtimes (milliseconds)										
"Simple" inversion	0.055	0.054	0.053	0.053	0.055	0.056	0.055	0.054	0.054	0.054
SVD	1.3	1.4	1.4	1.4	1.4	1.4	1.3	1.3	1.3	1.4
Iteration	1800	590	750	750	570	510	1100	520	440	590
Table 1.2: χ^2 between observations from model and estimated DEM										
"Simple" inversion	0	0	0	0	0	0	0	0	0	0
SVD	0	0	0	0	0	0	0	0	0	0
Iteration	0.10	0.11	0.003	4.3	19.6	0.038	3.2	0.009	67.4	0.11
Table 1.3: Cross-correlation coeff. between model and estimated DEM										
"Simple" inversion	0.75	0.063	0.098	0.54	0.048	0.069	0.22	-0.096	0.053	0.069
SVD	0.89	0.95	0.92	0.67	0.72	0.69	0.54	0.99	0.95	0.89
Iteration	1.00	1.00	1.00	0.56	0.42	0.64	0.48	1.00	0.99	0.99

Table 1: Quantitatively comparing DEM reconstruction methods for different DEM models. Models {a,b,c} are Gaussian distributions for cool, warm, and hot plasma. Models {d,e,f} are "double isothermal" peaks for cool, warm, and hot plasma. Model g is a cool isothermal peak plus a hot isothermal peak. Models {h,i} are multithermal. The median values are simply the medians for this arbitrary set of nine models.

$\sim 400 \times \tau(\text{SVD}) \sim 10^4 \times \tau(\text{"Simple" inversion})$.

The second tabulated quantity is the χ^2 fit to the observations. Note that inversion methods reproduce the observations perfectly. This is a mathematical consequence when solving a well-determined (or underdetermined) system of equations. Iteration converges to the first minimum it reaches from the starting guess, which may only be a (nonzero) local minimum in χ^2.

The third tabulated quantity is the cross-correlation coefficient between the input and solution DEMs. The iterative method is shown to most accurately reconstruct the DEMs, typically. "Simple" inversion does not have the temperature resolution to accurately reproduce the input DEMs. The SVD method does a fair job, considering that the principal solution is only one of a family of solutions, some of which might be much better. (In fact, since we are solving over the same temperature bins for which the input DEMs are defined, the input DEM is definitely a member of the SVD family of solutions. Of course, this would not be expected when analyzing observations of coronal plasma.) From these results, it is apparent that the iterative approach does well at reproducing our sample of model DEMs, giving positive solutions. Its ability to reproduce the observations (in terms of the χ^2 statistic) varies greatly. The inversion methods are much faster, which is a prominent concern when designing a DEM data product for, *e.g.*, the AIA, which produces images with 16+ Mpix at a cadence of 10 seconds. The SVD principal solution reproduces the observations perfectly (before error analysis), and does almost as good a job at reconstructing the DEM models as the iterative method does, although it can return negative components. There is freedom to impose some physical constraints on inversion methods (such as positivity) while retaining computation speeds, by allowing the χ^2 statistic to go to N_i.

2.5 Sixteen Million DEMs Every Ten Seconds

Calculating DEMs at several points in an image is straightforward for nearly any method, however the true power of large field of view DEM observations comes when the DEMs are available for every image set. Say, for example, there is a coronal loop visible in a few adjacent channels, and we wish to test the hypothesis that the loop is isothermal. With AIA standard cadence we can follow the evolution of this loop from appearance to disappearance with a ten second cadence. If the loop lasts for 100 minutes we will have an observational dataset that consists of 600 sets of 6 EUV images to form DEMs from. For this project we would limit our analysis to the few hundred pixels surrounding the loop, say 1/4 million pixels/frame total. It is apparent that if the visible loop is in fact a physically distinct structure in the corona, its evolution will be different from the surrounding plasma. There will be "features" within the loop's DEM that will evolve together; the rest of the DEM in the loop can be attributed to changes along the line of sight, not associated with the loop in question. An isothermal loop will have a DEM feature that is within the temperature resolution of the telescopes used ($\sim 0.2 \log T_e$). The ability

13

to calculate DEMs at every point along a loop (and all adjacent points, too) will provide an unprecedented set of observational constraints on coronal loop models and corona heating theories. As shown in Table 1.1, the run times for SVD are about 400 times faster than the iterative method. However, the iterative method provides a better fit to the DEMs. The iterative model depends on an initial guess of the DEM; if we are clever in our choice of the first guess maybe the runtime for the iterative model can be improved. In the cases described above a flat curve was used as the initial guess. Can we speed up the reconstruction for a time series of mega-pixel images via a "pre-conditioned" guess that takes advantage of the shared DEM information contained within mega-pixel images? Four methods are compared: *Brute Force* - our standard method; for each image, solve for the DEM of each pixel independently using a flat first guess. *Single Average* - for each image, average all pixels and calculate a "global" DEM; use this as a first guess for the DEM reconstruction of each pixel. *Time Dependent* - for the first image, solve for the DEM of each pixel independently using a flat first guess; use the resulting DEMs as a first guess for calculations in second image; iterate to last image. *Time Averaging* - for first image, use a global DEM as a first guess for DEM reconstruction for each pixel; use the resulting DEMs as a first guess for calculations in second image; iterate to last image.

3 Electronic Systems

The TXI rocket Electronic system has four prime functions:

1: Control the operation of a E2V 42-40 CCD detector. This would include the external shutter for exposure and readout sequencing.
2: Control the operation of the TXI monochromator for wavelength selection.
3: Control of the detector and H/K data.
4: Control of the command instruction.

The electronic design unitizes an on-board single board computer (SBC). It is partitioned for prime science operations (detector image data) and for the command, housekeeping, and instrument operations. The SBC is a Kontron 845D, running on a passive PCI Bus back plane. The SBC has two serial ports for command and housekeeping telemetry, an Ethernet port for ground diagnostics, and a Compact Flash disk to increase boot-up speed. The flight software will be based upon existing code written in C++ and will run on a Windows NT operating system. The SBC will control the image acquisition of the Moses 42-40 CCD detector.

After appropriate processing and formatting by a dedicated PCI frame grabber board (Moses #30259), the SBC utilizing a packet protocol with error-correcting capabilities will transfer images to the rocket telemetry interface. The software will run a pre-programmed image sequence but will be able to accept real-time commands to change the sequence based upon quick look data. The data transmission is supplied by a NASA 10 Mbit downlink system for real time viewing during the flight. The data are also stored on-board for post-flight retrieval should data transmission fail, or have excessive dropouts. A GSE system will have four main functions: displaying of real-time thumbnails of

14

the data, displaying of full images as telemetry constraints allow, displaying of housekeeping telemetry, and a command uplink to control image sequencing and exposure levels. Both the flight and GSE systems will require only minimal modifications to their original TXI designs.

The TXI system block diagram (Fig. 9) shows the TXI electronic system. NASA supplies the command telemetry, data telemetry, telemetry interface, flight batteries, and video telemetry for the H*alpha* camera. NASA will provide and service the flight batteries. A latching changeover relay will switch the experiment between external and internal power; this will be under NASA control. The experiment's battery power will be applied at two minutes before launch. External power will be used for all testing, except for flight system tests.

3.0.1 The High Resolution X-ray (HRX) Imaging Detector

For the past decade our group at the Center for Astrophysics has been engaged in a program to design, build and fly high quality electronic imaging devices for soft x-ray and XUV applications. We have successfully flown a number of such devices in the NIXT rocket program, including intensified CCD cameras which have provided real-time images of the sun at He II λ304Å and Fe XII λ193Å. Under a NASA Grant, we developed the High Resolution X-ray (HRX) imaging detector, a CCD camera designed for flight and sensitive to both visible light and XUV wavelengths. This camera was flown succesfully in the previous TXI flight. For the past year we have been working with the DLR in Berlin, Germany to develop a larger-format camera, which will be available during the current calendar year for flight in the rebuilt TXI.

The new HRX camera uses a back-illuminated E2V 42-40 CCD (with no anti-reflection coating). This is a 2Kx2K device, with 13.5μ pixels. The DQE at the TXI wavelengths is $\approx$ 85% (as measured at SAO), since we are working below the silicon L-edge. This is substantially better than the efficiency of either photographic emulsions or of phosphor coated CCDs. The readout noise level with moderate cooling (–60°C) is 20 e$^-$ per pixel at a readout rate of 1,00,000 pixels/sec, so that a high-quality image requires an average exposure of only $\approx$250 e$^-$ per pixel. The large-format CCD camera is used to provide the main TXI images, and a video-format camera provides a real-time Hα image.

The flight version of the HRX camera is shown in Fig. 10.

3.1 Affiliated Scientists

As part of our overall approach, which has historically included extensive collaborative arrangements with scientists outside of the Smithsonian, we have initiated specific collaborations for the work described in this proposal. Travel support for visitors is in most cases provided by internal SAO funding.

The following list gives the names of the individuals who will be working with us and a brief description of the role each will play in this program.

Dr. G. Peres, Osservatorio di Palermo. Will

15

participate in data analysis with emphasis on modelling of coronal structures using the FLASH code, for which they are co-developers; he will also provide participation by members of the Osservatorio staff and students from the U. of Palermo.

Prof. R. Rosner, U. of Chicago. Will provide expertise in implementation of the FLASH loop modelling code at SAO, will participate in the data analysis and will involve students from U. of Chicago in the analysis.

Dr. B. Schmieder, IAP Medoc, will coordinate observations simultaneous with the TXI launch, at the newly-upgraded Pic du Midi Observatory; science programs will focus on coronal dynamics on a target-of-opportunity basis.

Dr. N.O. Weiss, DAMTP (Cambridge, UK). Will provide theoretical analysis of coronal data in the area of magneto-convection, studies of sunspot structure and dynamo-related global analysis; emphasis will be on the flows in penumbral loops seen at 10^6 K.

3.2 Impact of This Work

The Tunable XUV Imager (TXI) is a new concept in coronal imaging, which opens up new possibilities for scientific studies. For the first time we will be able to obtain high spatial resolution imaging in isolated individual emission lines, while also being able to observe a large number of successive ionization stages of the same element; thus *all* of the coronal plasma within the covered temperature range will be observed. In addition, the same telescope can be used to obtain velocity maps and polarization maps at any desired wavelength.

The TXI permits us to address, among others, the following questions:
– What is the distribution of temperature and emission measure in the corona, and how is it structured?
– Where are plasma flows present in the corona, and what is their magnitude?
– Where is XUV emission from the hot coronal plasma polarized, and by how much?

The answers to these questions are directly relevant to determining the coronal heating mechanism(s), and to establishing the reasons for instability in coronal structures. We anticipate that the TXI concept will lead to fundamental advances in our understanding of coronal physics, especially when used with a high resolution, large format detector, and eventually from a platform capable of carrying out observations over an extended time period.

The TXI will provide support and help in planning observing programs for several NASA missions, such as TRACE, Solar Probe and STEREO, since it observes coronal emission lines which are not available to the imaging instruments on those satellites, and it provides images for spectroscopic instruments. The types of emission measure, temperature, velocity and polarization data obtained from TXI are of potential usefulness to RHESSI, especially if we launch the sounding rocket payload as part of a flare-wait campaign, so that the TXI is observing during a flare.
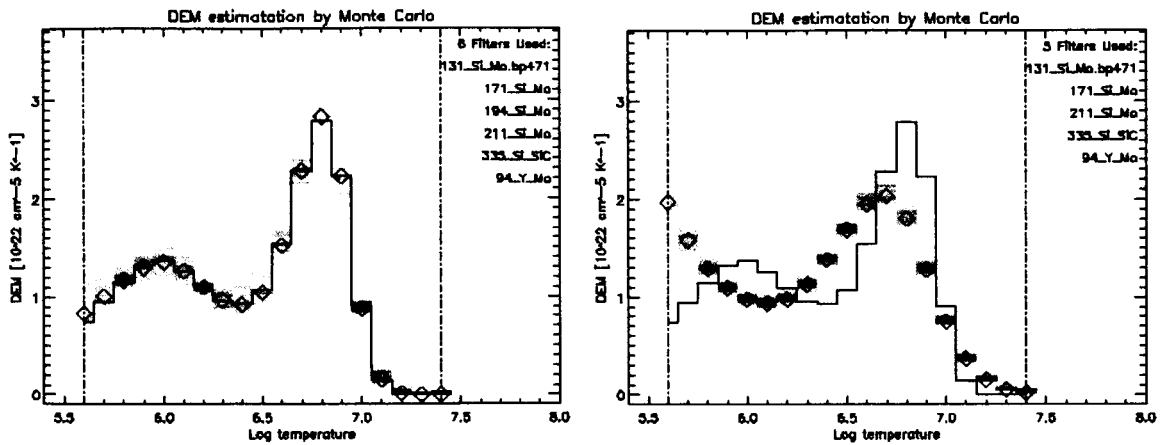
Figure 8: The number of independent channels used in the DEM reconstrcution is crucial: reducing the number from 6 to 5 introduces are large degradation in the quality of the reconstruction.
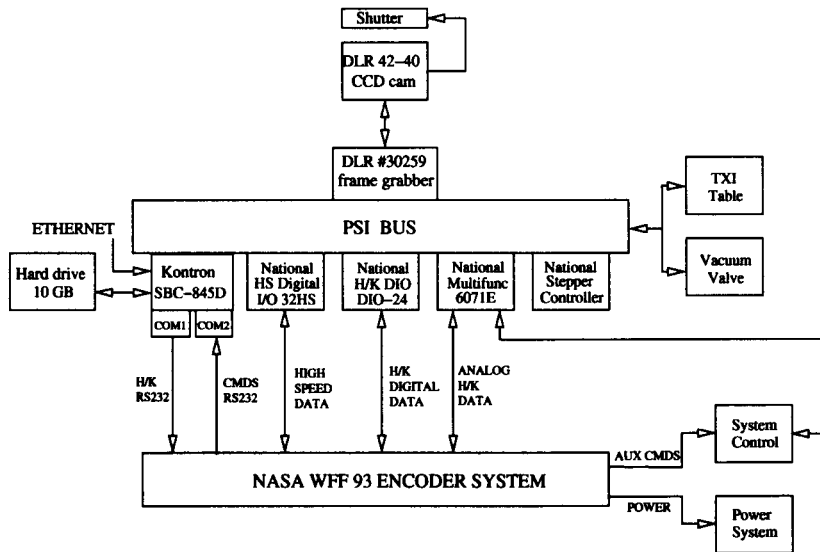
Figure 9: Schematic block diagram of the TXI electronics system.
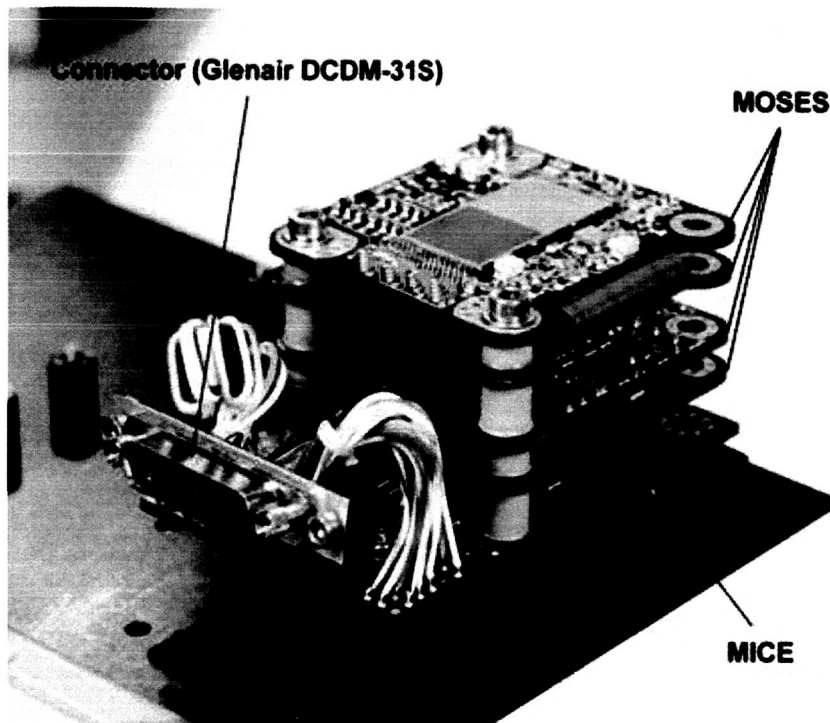
Figure 10: The HRX camera utilizes an efficient compact design for flight applications.

4 References

Aschwanden, M.J., etal. 2000a, *Ap. J.* **531**, 1129.

Aschwanden, M.J., etal. 2000b, *Ap. J.* **541**, 1059.

Aschwanden, M.J., J.C. Brown and E.P. Kontar 2002, *Sol. Phys.* (in press).

Cargill P.J. & Priest, E.R. 1980, *Solar Phys.*, **65**, 251.

Cowan, P.L., T.J. Hasting, J.P. Kirkland 1983, *Nucl. Instr. Methods* **208**, 349.

Craig, I.J.D. & McClymont A.N. 1986, *Ap. J.* **307**, 367.

Dere, K. et al. 1987, *Solar Phys.* **114**, 223.

Glencross, W.M. 1980, *A. & A.*, **83**, 65.

Golub, L. & Pasachoff 1997, *The Solar Corona*, Cambridge University Press, Cambridge, UK.

Golub, L., E.E. DeLuca, M.A. Weber and A. Sette 2004, *Proc. IAU Symposium 223*, eds. Stepanov etal.

Guhathakurta, M. & Fisher, R.R. 1995, *Geophys. Res. Lett.* **22**, 1841.

Koutchmy, S. et al. 1994, *Third SOHO Workshop: Solar Dynamic Phenomena and Solar Wind Consequences*, p. 139; ESA, ESTEC, Noordwijk, The Netherlands.

Landini, M. & Mosignori Fossi, B.C. 1981, *A & A* **102**, 213.

Lenz, D. etal. 1999, *Ap. J.* **517**, L155.

Linford, G.A. and Wolfson, C.J. 1988, *Ap. J.* **331**, 1036.

Martens, P.C.H. etal. 2000, *Ap. J.* **537**, 471.

Meyer, F. & Schmidt, H.U. 1968, *Zeits. fur Angewandte Mathematik und Mechanik*, **48**, T218.

Noci, G. 1981, *Solar Phys.* **69**, 63.

Parker, E.N. 1994. *Spontaneous Current Sheets in Magnetic Fields*, Oxford University Press, NY.

Poland, A.I. 1994, *Third SOHO Workshop: Solar Dynamic Phenomena and Solar Wind Consequences*, p. 227; ESA SP-373, ESTEC, Noordwijk, The Netherlands.

Poletto, L., Boscolo, A., Pelizzo, M.G., Placentino, L. and Tondello, G. 1994. Opt. Eng., 33, 2544.

Priest, E. 1993, in *Physics of Solar and Stellar Coronae*, p. 515, eds. J. Linsky and S. Serio, Kluwer Academic Publishers, Dordrecht, Holland..

Rosner, R., W.H. Tucker and G.S. Vaiana 1978, *Ap. J.*, **220**, 643.

Schmelz, J.T. etal. 2001, *Ap. J.* **556**, 896.

Takeda, A., H. Hurokawa, R. Kitai and K. Ishiura 1994, p. 381 in Proc. Kofu Symposium, NRO Report No. 360, eds. S. Enome and T. Hirayama.

Takeda, A., et al. 1995, in Proc. IAU Symp. 153, eds. Y. Uchida, T. Kosugi and H. S. Hudson, Kluwer Academic Publishers, Dordrecht, Holland.

Tarbell, T.D., Bruner, M., Jurcevich, B., Lemen, J., Strong, K., Title, A., Wolfson, J., Golub, L., and Fisher, R. 1994. *Proc. 3rd SoHO Workshop*, ESA SP-373.

Yoshida, T., S. Tsuneta, L. Golub, K. Strong and Y. Ogawara 1995, *Publ. Astron. Soc. Japan*, **47**, L15.

Walker, A.B.C., R.B. Hoover and T.W. Barbee, Jr. 1993, in *Physics of Solar and Stellar Coronae*, op. cit. , p. 97.

Winebarger, A.R., DeLuca, E.E. and Golub, L. 2001. *Ap. J.* **553**, L81.